Biophysical Journal
Article

Biophysical Society

Interfacial behavior of phospholipid monolayers revealed by mesoscopic simulation

Yongzheng Zhu,[1,2,3] Xuan Bai,[1] and Guoqing Hu[1,*]
[1]Department of Engineering Mechanics, State Key Laboratory of Fluid Power and Mechatronic Systems, Zhejiang University, Hangzhou, China; [2]The State Key Laboratory of Nonlinear Mechanics, Institute of Mechanics, Chinese Academy of Sciences, Beijing, China; and [3]School of Engineering Science, University of Chinese Academy of Sciences, Beijing, China

ABSTRACT A mesoscopic model with molecular resolution is presented for dipalmitoyl phosphatidylcholine (DPPC) and palmitoyl oleoyl phosphatidylcholine (POPC) monolayer simulations at the air-water interface using many-body dissipative particle dynamics (MDPD). The parameterization scheme is rigorously based on reproducing the physical properties of water and alkane and the interfacial property of the phospholipid monolayer by comparison with experimental results. Using much less computing cost, these MDPD simulations yield a similar surface pressure-area isotherm as well as similar pressure-related morphologies as all-atom simulations and experiments. Moreover, the compressibility modulus, order parameter of lipid tails, and thickness of the phospholipid monolayer are quantitatively in line with the all-atom simulations and experiments. This model also captures the sensitive changes in the pressure-area isotherms of mixed DPPC/POPC monolayers with altered mixing ratios, indicating that the model is promising for applications with complex natural phospholipid monolayers. These results demonstrate a significant improvement of quantitative phospholipid monolayer simulations over previous coarse-grained models.

SIGNIFICANCE Quantitative study on phospholipid monolayers at the air-water interface is crucial to understand the biophysics of cell membranes and lung surfactants. However, it remains challenging to quantitatively model the phospholipid monolayers at the mesoscopic scale limited by the scale of all-atom molecular dynamics (AAMD) simulations and the defect in the surface tensions of coarse-grained (CG) MD simulations. Herein, we proposed a mesoscopic model for dipalmitoyl phosphatidylcholine and palmitoyl oleoyl phosphatidylcholine monolayers at the air-water interface using many-body dissipative particle dynamics (MDPD). The interfacial and mechanical properties and the molecular structure derived by MDPD phospholipid monolayers are quantitatively in line with the AAMD simulations and experiments, which demonstrates a significant improvement over previous CGMD simulations.

INTRODUCTION

Lipid monolayers at the air-water interface are of interest in a variety of disciplines. Through the correspondence between the lipid monolayer and bilayer, the interpretation of the lipid bilayer properties can be obtained from lipid monolayer experiments, which are more easily performed than bilayer experiments (1–4). An exemplary case of monolayer is the lung surfactant monolayer. Lung surfactant is composed of hundreds of lipids (~90% by weight), mainly dipalmitoyl phosphatidylcholine (DPPC) and unsaturated phosphatidylcholines (PCs), and four types of surfactant proteins (~10% by weight) (5–7). It can adsorb on the surface of the alveolar fluid that reduces the surface tension of the alveoli to maintain tidal respiration (8,9).

Studying the structure and mechanical properties of the lipid monolayer during compression and expansion is central to elucidating the biophysics of lung surfactant (10–12). Experimental studies can measure the phase coexistence, compressibility, and surface tension of the lipid monolayer through atomic force microscopy, Langmuir-Blodgett balance, the captive bubble method, and other techniques (13–17). However, although it is still difficult to directly study and observe the mesoscopic details through these experiments, these can be obtained from molecular dynamics (MD) simulations (18–21).

At present, the commonly used MD methods for biomembrane include all-atom (AA) MD and coarse-grained (CG) MD (22). Although AAMD methods such as the

Submitted April 9, 2021, and accepted for publication September 20, 2021.
*Correspondence: ghu@zju.edu.cn
Yongzheng Zhu and Xuan Bai contributed equally to this work.
Editor: Siewert Jan Marrink.
https://doi.org/10.1016/j.bpj.2021.09.031

CHARMM force fields (23) have high simulation accuracy, they require tremendous computing resources and time to simulate biological systems with a spatial scale of more than tens of nanometers and thus are not suitable for simulating the mesoscopic phenomena of the lipid monolayer. In CGMD simulations, clusters of atoms are considered beads that interact with each other, therefore decreasing the freedom of the total atoms and saving lots of computing costs. Nowadays, Martini force field CGMD (24,25) and dissipative particle dynamics (DPD) (26) are the two most popular CGMD methods for biological systems. The famous Martini force field provides systematic force field parameters for commonly used lipids and other biological molecules and thus is suitable for modeling the complex lipid monolayers at the air-water interface. However, the Martini water model underestimates the air-water surface tension because of the narrow well of the Lennard-Jones potential, which is flawed for modeling interfacial adsorption, pore formation, and the pressure-area isotherm of the monolayers (27). The Shinoda model (28,29) and the Chiu-Scott-Jakobosson water model combined with the Martini force field (9,30) have achieved good results on presenting the pressure-area isotherms of DPPC. These pioneering works have encouraged us to improve the numerical models for better simulation of the phospholipid monolayers at relatively large scale. DPD was initially proposed for simulating complex fluids at the mesoscopic scale and has also been widely used for biomembrane simulations (31). Compared to the Martini force field, DPD has a soft potential that allows a larger timestep in simulations and is more suitable for modeling mesoscopic thermodynamics because of the included dissipative forces and random forces (32). However, the accuracy and universality of DPD are normally inferior to the Martini force field model. Most importantly, DPD cannot handle the problems of the air-water interface because of the absence of attractions in its interaction potential.

Many-body (or multibody) DPD (MDPD) modifies the original DPD by replacing the purely repulsive conservative forces with forces deriving from a many-body potential (33). In this way, the equation of state has a higher-order pressure-density curve to accommodate vapor-liquid coexistence than DPD models. Thus, the conservative force of MDPD was modified to be related to density (34). The conservative force of MDPD was further developed by adding a pair of soft attractive interactions with a larger cutoff radius than the repulsive interactions (35). Recently, MDPD has been used for studying the adsorption behavior of surfactants with simple chemical structure such as sodium dodecyl sulfate (36,37). However, it is still difficult to use the MDPD model for quantitative lipid simulations.

Herein, we propose an MDPD model for two commonly used phospholipids, namely DPPC and palmitoyl oleoyl phosphatidylcholine (POPC), for lipid monolayer simulations. The parameterization for the lipid models is rigorously based on reproducing the experimental density and surface tension of reference systems (water and alkane) and the surface pressure-area isotherm of the lipid monolayer. Then, we examine the mechanical property (compressibility modulus) and the molecular structures, including pore formation, collapse, thickness, and order parameter, of the modeled lipid monolayers by comparison with experiments and other simulations. Finally, we extend the model to simulate the mixed DPPC/POPC monolayer at different ratios and obtain the pressure isotherm in good agreement with the experimental results, showing the versatility of this scheme.

MATERIALS AND METHODS

MDPD simulations

Theory and algorithm

The motion of the MDPD particles is described according to Newton's second law, and the total force $\mathbf{F}_i$ on the bead i over all beads j within certain cutoffs consists of conservative force $\mathbf{F}_{ij}^C$, dissipative force $\mathbf{F}_{ij}^D$, and random force $\mathbf{F}_{ij}^R$:

$$\frac{d\mathbf{v}_i}{dt} = \mathbf{F}_i = \sum_{i \neq j} \left(\mathbf{F}_{ij}^C + \mathbf{F}_{ij}^D + \mathbf{F}_{ij}^R \right). \tag{1}$$

The conservative force of this expression is represented as (35)

$$\mathbf{F}_{ij}^C = A_{ij}\omega_c\left(r_{ij}\right)\mathbf{e}_{ij} + B_{ij}\left(\overline{\rho}_i + \overline{\rho}_j\right)\omega_d\left(r_{ij}\right)\mathbf{e}_{ij}, \tag{2}$$

where the first term with a matrix of attraction amplitudes A_{ij} stands for an attractive interaction within a range $r_c = 1$, and the second many-body term with a matrix of repulsion amplitudes B_{ij} is the density-dependent repulsive interaction within a short range $r_d = 0.75$. There is a no-go theorem that constraints the condition for the parameters of the multicomponent system, which means the force law is not conservative unless B_{ij} is a constant matrix (38). Therefore, a single repulsion parameter B can be used to replace B_{ij}. The weight function is $\omega_c = 1 - r_{ij}/r_c$ for $r_{ij} \leq r_c$ and $\omega_c = 0$ for $r_{ij} > r_c$ and $\omega_d = 1 - r_{ij}/r_d$ for $r_{ij} \leq r_d$ and $\omega_d = 0$ for $r_{ij} > r_d$. The local density of the repulsive term is defined as $\rho_i = \sum_{i \neq j} \omega_\rho(r_{ij})$ for each particle, and the generalized weight function is expressed as (35)

$$\omega_\rho(r) = \frac{15}{2\pi r_d^3}(1 - r/r_d)^2. \tag{3}$$

The dissipative and random forces are defined, respectively, as

$$\mathbf{F}_{ij}^D = -\gamma\omega_D\left(r_{ij}\right)\left(\mathbf{e}_{ij} \cdot \mathbf{v}_{ij}\right)\mathbf{e}_{ij} \tag{4}$$

and

$$\mathbf{F}_{ij}^R = \delta\omega_R\left(r_{ij}\right)\xi_{ij}\Delta t^{-1/2}\mathbf{e}_{ij}, \tag{5}$$

where γ is the dissipative parameter, ξ_{ij} is a random variable conforming to a Gaussian distribution, $\mathbf{e}_{ij} = \mathbf{r}_{ij}/r_{ij}$, and $\mathbf{v}_{ij} = \mathbf{v}_i - \mathbf{v}_j$. The system satisfies the Gibbsian equilibrium and the fluctuation-dissipation theorem (39) if the dissipative parameter γ and the amplitudes of random force δ satisfy $\delta^2 = 2\gamma k_B T$ and the weight function follows $\omega_D(r) = [\omega_R(r)]^2$. The combined effect of dissipative force and random force acts as a thermostat.

CG models of phospholipids

In the classic DPD CG strategy developed by Groot (31), one water bead (W) corresponds to three water molecules. Thus, the number $N_m = 3$ can be considered the CG degree of the model. At this CG degree, the value of the repulsive parameter B in these MDPD simulations was fixed at 25 (35,38). Inspired by the CG schemes in the Martini force field (24), the CG model of DPPC has two hydrophilic head beads (H) representing the phosphate moiety and the choline moiety, two backbone beads (G) representing the glycerol linkage, and five hydrophobic tail beads (T/C1) at each tail with each bead corresponding to three carbon atoms. Note that the CG degree of lipid tails is the same as that of the MDPD water, which is different from the Martini CG degree (Fig. 1 *A*) (24,40). The only difference between the CG models of POPC and DPPC is the bead type of the second bead near the glycerol linkage on the main tail chain because of the presence of an unsaturated bond in POPC. Therefore, this carbon bead containing a double bond was redefined as type T/C2.

Bonded interactions between connected beads are represented by a weak harmonic potential. Following Groot and Gao (31,41), bonds are described by $V_{\text{bond}}(r) = (1/2)K_{\text{bond}}(r - r_0)^2$ with an equilibrium bond distance $r_0 = 0.45r_c$, and a force constant of $K_{\text{bond}} = 400\ k_BT/r_c^2$ is applied on all neighboring beads except for the glycerol linkage bead ($r_0 = 0.40r_c$). Angles are described by $V_{\text{angle}}(\theta) = \frac{1}{2}K_{\text{angle}}(\theta - \theta_0)^2$ for three adjacent beads. A force constant of $K_{\text{angle}} = 4\ k_BT/rad^2$ and an equilibrium value of the angle $\theta_0 = 180^\circ$ are applied to two head beads connected to one glycerol bead, the second head bead connected to the first glycerol bead and tail bead, a glycerol bead connected to two tail beads, and three consecutive tail beads; for two glycerol beads connected to a head bead or tail bead, $K_{\text{angle}} = 4\ k_BT/rad^2$ and $\theta_0 = 120^\circ$; for the angles involving the *cis* double bond, $K_{\text{angle}} = 6\ k_BT/rad^2$ and $\theta_0 = 120^\circ$. For two glycerol beads connected to the first bead of the sn-1 tail chain, the angle was set to $K_{\text{angle}} = 4\ k_BT/rad^2$ and $\theta_0 = 100^\circ$ in the DPPC model, but $K_{\text{angle}} = 1\ k_BT/rad^2$ in the POPC model.

System setup

For calculations of the surface tension at the air-water interface, the simulation setup (Fig. 1 *B*) included a small water cube of $8 \times 8 \times 10\ r_c$ containing 4352 water beads in an $8 \times 8 \times 20\ r_c$ simulation box and a large water cube of $30 \times 30 \times 10\ r_c$ containing 61,200 water beads in a $30 \times 30 \times 30\ r_c$ simulation box. To determine the interaction parameters of the tail beads and water, 774 hexadecane (C5) molecules or 968 dodecane (C4) were placed in an $8 \times 8 \times 20\ r_c$ box with an ensemble. In the simulation of coexistence of oil and water phase (Fig. 1 *B*), a water slab containing 4352 water beads and two boundary oil slabs containing 840 hexadecane (C5) molecules were placed in a box of the same size.

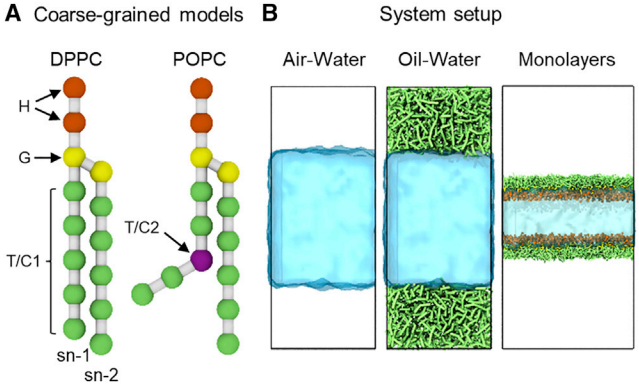

FIGURE 1 (*A*) CG MDPD models for DPPC and POPC molecules. Orange, yellow, and green beads represent head (H), glycerol (G), and tail (T) beads, respectively. (*B*) Setups for calculations of water-air, water-oil, and phospholipid monolayer surface tensions. To see this figure in color, go online.

For monolayer simulations, we simulated DPPC, POPC, and mixed DPPC/POPC monolayers. The simulation setup of the monolayer included a water slab with two air-water interfaces that were covered by two symmetrical monolayers (Fig. 1 *B*). For mixed DPPC/POPC monolayers, DPPC and POPC were mixed at three molar ratios of 1:3, 1:1, and 3:1. For all the above phospholipid monolayers, the small system contained 444 molecules per monolayer and 21,792 water beads; the large system contained 4000 molecules per monolayer and 196,128 water beads. To obtain the surface pressure-area isotherms, a series of initial structures of lipid monolayers with different values of area per lipid (APL) were generated by controlling the lateral box size using the PACKMOL package (42). The lateral size of the small box is in the range of 15–25 r_c, and the large box is in the range of 45–75 r_c.

Surface pressure-area isotherm calculation

The surface pressure-area isotherm is given by a series of surface pressure points corresponding to the relation $\pi(a) = \gamma_0 - \gamma(a)$, where γ_0 denotes the surface tension of the air-water interface. The surface tension in the monolayer, γ, is calculated from the differences in the normal pressure P_N and lateral pressure P_L in the box according to the Irving-Kirkwood approach (43), expressed as $\gamma = (P_N - P_L) \times L_z/2 = (P_{zz} - (P_{xx} + P_{yy})/2) \times L_z/2$, where L_z is the size of the box in the normal direction and P_{xx}, P_{yy}, and P_{zz} are the ensemble-time average of pressure components in the x, y, and z directions, respectively. Each point of the surface pressure-area isotherm was obtained from one independent simulation at the constant area. The points of the surface pressure-area isotherm were obtained once the calculated ensemble-time averaged surface tension stabilized, i.e., the simulated phospholipid monolayer reached a metastable or quasiequilibrium state.

Simulation details

All simulations were performed using the Meso-DPD module in the LAMMPS package (44,45). Note that the original Lucy kernel function in the MDPD package was replaced by Eq. 3 to calculate the local density. All simulations were performed in a three-dimensional box with periodic boundary conditions in all directions. The time step was set to $\delta t = 0.01$ with the MDPD time unit and the equilibration simulation was sustained by 1,000,000 time steps for small systems and 10,000,000 time steps for large systems to ensure simulation convergence. The criterion for convergence is that the calculated surface tension remains constant over a long period of time. All simulations were carried out at 300 K using the NVT ensemble. The visualization of molecular configurations and simulation results was performed using the VMD software (46).

Constrained drop surfactometry experiments

Monolayer formation

DPPC (purity >99%) and chloroform ($CHCl_3$, purity >99%) were purchased from Avanti Polar Lipids (Alabaster, AL). POPC (purity >99%) was purchased from Sigma-Aldrich (St. Louis, MO). Phospholipids for the experiments were used without further purification. Ultrapure water (pH 7.4) from the Millipore Simplicity water purification system was used in all experiments. First, 20 mg DPPC or POPC was dissolved in 20 mL chloroform to form 1 mg/mL DPPC or POPC stock solutions, respectively. DPPC/POPC mixture stock solutions were prepared according to the molecular weights of DPPC (734.04) and POPC (760.08). The molar ratios of DPPC/POPC were 1:3, 1:1, and 3:1. Subsequently, an ultrasonic water bath was used to sonicate all prepared stock solutions at 25°C and 40 kHz for 5 min to obtain a series of uniformly mixed stock solutions. The droplet (~15 μL volume) was constrained on a hydrophilic pedestal (~3 mm in diameter) that uses its knife-sharp edge to prevent film leakage and to maintain the droplet integrity. A small amount of stock solution (1 mg/mL) was spread onto the droplet using a microsyringe. Then, the

droplet could completely evaporate chloroform in 1 min without interference.

Surface pressure-area isotherm measurement

The droplet was slowly expanded to increase the surface tension (γ) of the monolayer until it was close to the surface tension (γ_0) of pure water. The spread lipid monolayer was subsequently compressed at a rate of 0.005 cm^2/s and the real-time profile images of the droplet were directly displayed in the Axisymmetric Drop Shape Analysis graphical user interface, processed, and analyzed to generate a series of real-time surface tension measurement values to obtain the complete compression pressure-area isotherm (47–49). Each measurement was repeated three times to ensure the accuracy and repeatability of the experimental results. All measurements were carried out at 300 ± 0.1 K.

RESULTS AND DISCUSSION

Parameterization of water and oil and lipid tail

We first calibrate the MDPD parameters for the water model by mapping the liquid phase properties of water to its actual physical properties and correlating the MDPD dimensionless units to the actual units. The interaction parameter A_{WW} of water beads is set to −50, following the previous MDPD water model that can consistently reproduce the interface properties of water (50). In the simulation results, the equilibrium number density of water beads in both the large and small boxes is 6.8 r_c^{-3}. One water bead represents three water molecules and the volume of one water molecule is 30 $Å^3$, which means that one water bead in a box occupies a real volume of 90 $Å^3$. According to the number density of the water beads in the box, the simulated characteristic length $r_c = 8.49$ Å is obtained, which determines the length scale of the system. In addition, the surface tension of water in the MDPD unit is 12.4 k_BT/r_c^2. From the simple scaling relations, the calculated density and surface tension of water are 997 kg · m^{-3} and 71.2 mN/m at a room temperature of 300 K, which is consistent with the experimental results. The calculated surface tensions of water at different temperatures are validated against the constrained drop surfactometry (CDS) measurements in Table S2. After the characteristic length of the simulation is determined, the timescale of the simulation is obtained through mapping the calculated diffusion coefficient D_{bead} of water to the experimental value $D_{water} = 2.43 \times 10^{-9}$ $m^2 \cdot s^{-1}$. Note that this calculated diffusion coefficient is corrected using the protocol of Yeh and Hummer (51). The correspondence between the MDPD parameters in dimensionless units and the actual physical values is shown in Table 1.

Note: physical properties r_c, ρ, γ, p, and δt correspond to the cutoff radius, density, surface tension, pressure, and time step, respectively. V is the volume of one water molecule, M is the molar weight of a water molecule, N_a is Avogadro's number, k_B is Boltzmann's constant, and T is 300 K.

Given that the monolayer surface tension is mainly dominated by the interactions tail-air and headgroup-water, we calibrate the parameters of the tail and head beads individually. The carbon atom in the saturated tail is similar to the one in the alkane compounds, such as hexadecane and dodecane. Thus, we compare the calculated bulk and surface properties of the alkanes with the experimental values to calibrate the parameters of the tail beads. The other beads of the lipid, including group beads, linkage beads, and unsaturated beads, are calibrated by directly comparing the calculated and experimental pressure-area isotherms of the lipid monolayer, which is shown in the next section.

TABLE 1 Correspondence between the MDPD parameters in dimensionless units and physical values

MDPD			Physical units
Parameter	Value	MDPD → real units	Value
Bead	1	N_m	3 H_2O
r_c	1	$(\rho N_m V)^{1/3}$	8.49 Å
ρ	6.8	$\rho N_m M/N_a r_c^3$	997 kg · m^3
γ	12.4	$\gamma k_B T/r_c^2$	71.2 mN · m^{-1}
p	0.1	$p k_B T/r_c^3$	6.75 MPa
δt	0.01	$N_m D_{bead} r_c^2/D_{water}$	0.46 ps

The hexadecane molecule model is divided into five CG beads, and the dodecane is divided into four beads. The bond length between two adjacent carbon beads is set to $0.45r_c$, bonding stiffness is 400 k_BT/r_c^2, and angular stiffness is 4 k_BT/rad^2 based on a previous model (41). The attraction interaction parameter A_{ij} is appropriately adjusted by fitting the density of the oil and the surface tensions of the oil-air and oil-water well with the experimental values. When A_{CC} is tuned to −23, the hexadecane-air surface tension is 26.6 mN/m and the density is 767 kg · m^{-3}; the dodecane-air surface tension is 25.6 mN/m, and the density is 756 kg · m^{-3}. When A_{WC} is set to −26, the hexadecane-water surface tension is 52.8 mN/m. These results are in good agreement with experimental values (52). Surface tensions between different phases are shown in Table 2.

Surface pressure-area isotherms of the DPPC and POPC monolayers

After determining the interaction parameters between carbon beads (T/C1) and water beads (W), we screen the parameters of other beads within a reasonable interval to determine the interaction parameters. The DPPC monolayer in the small system is simulated to obtain a group of pressure-area isotherms with a series of parameter sets that are compared to the experimental results (Fig. S1 *A*). In this way, we can determine a set of parameters that fits the

TABLE 2 Interfacial tension between different phases

System	MDPD	Martini	Experimental
Water-air	71.2	32.0	72.0
Dodecane-air	25.6	25.3	24.0
Hexadecane-air	26.6	27.2	27.3
Hexadecane-water	52.8	55.2	53.0

Interfacial tension measured in mN/m.

calculated isotherm well with the experimental one. After parameters of the head beads and the linkage beads are calibrated, the parameterization of the T/C2 beads of the POPC molecule can be obtained through the same methods (Fig. S1 *B*). The nonbonded interaction parameters for all pairs of beads are shown in Table 3.

The calculated surface pressure-area isotherm of the DPPC monolayer is shown in Fig. 2 *A* with the isotherms determined by other techniques. There are four main phase regions in the calculated isotherm. When the APL is larger than 0.9 nm^2, the monolayer in the liquid-expanded (LE) phase coexists with pores (the corresponding snapshot is shown in Fig. 2 *B*). At this stage, the surface pressure is reduced to near 0 mN/m and the APL is 0.9 nm^2, which is much more coincident with the experimental and AAMD results than the Martini force field. When the APL ranges from 0.9 to 0.65 nm^2, the DPPC monolayer is in the LE phase with no pores and the lipid tails are mainly disordered (Fig. 2 *C*). As the APL continues decreasing (0.65–0.5 nm^2), the isotherm reaches a plateau and the slope of the isotherm fluctuates around zero, indicating a coexistence of LE and liquid-condensed (LC) phases (Fig. 2 *D*). The plateaus obtained by these MDPD simulations fit the experiments (15,53) and the AAMD simulations (54) more closely than the Martini simulations (12). For the APL range of 0.55–0.45 nm^2, the monolayer is in the LC phase and the tails are ordered (Fig. 2 *E*). However, the slope of the isotherm in the LC phase is much larger than that of the experiments, probably because of some inaccuracy of the force field and the NVT ensemble that leads to the large forces between the overlapped CG particles (55,56). As the surface pressure reaches 70 mN/m, that is, the surface tension is 0 mN/m, the monolayer is unstable and collapses with the lipids extruded to the water phase to form a micelle structure (Fig. 2 *F*). In general, the pressure-area isotherm with the corresponding monolayer morphology determined by the MDPD simulations is more coincident with the experimental results than the Martini force field (12). In addition, the calculated pressure-area isotherms of different sizes of monolayers using these MDPD simulations are consistent, which is somehow advantageous over the traditional AAMD and CGMD methods in simulating the lipid membranes because of the artificial rigidity and suppressed undulations in small systems (57–59).

Slightly different from the DPPC molecule, the POPC molecule has one unsaturated C=C bond in one of its tails and increases the disorder of the tails. Simulated MDPD and experimental CDS pressure-area isotherms are shown in Fig. 3 *A* and compared to AAMD (54) and several experimental isotherms (60–62) at the same temperature. In the APL range of 0.45–1.15 nm^2, the surface pressure of the POPC monolayer is higher overall than that of the DPPC monolayer at the same APL (Fig. S2). The POPC monolayer is more stable than the DPPC monolayer at low surface pressure, and the pore formation starts at APL = 1.0 nm^2 (Fig. 3 *B*). In addition, the POPC monolayer is always in the LE phase at 300 K (Fig. 3, *C* and *D*) because of the unsaturated chains in the POPC molecules.

TABLE 3 MDPD bead-pair nonbonded interaction parameters

A_{ij}	W	H	G	T/C1	T/C2
W	−50	−51	−48	−26	−30
H	−51	−37	−34	−30	−32
G	−48	−34	−34	−27	−27
T/C1	−26	−30	−27	−23	−21
T/C2	−30	−32	−27	−21	−23

The calculated DPPC isotherms at different temperatures are shown in Fig. 4 *A* to validate against the previous experiment data (63). The temperature clearly affects the calculated isotherms near the LE-LC coexistence phase but only slightly affects the high and low surface pressure region in the isotherms, which is similar to the existing experimental measurements (15,64,65). In particular, an increase in temperature leads to an upward shift and a shortened plateau related to the LE-LC coexistence. When the temperature is higher than the main phase transition temperature of DPPC (314 K), the LE-LC coexistence phase disappears and only the LE phase is left, as confirmed by the molecular structures (Fig. 4, *B–D*). Similarly, the shapes of POPC isotherms at the temperatures above the main phase transition temperature (273 K) are almost identical (Fig. S3). In addition, our model can also capture the temperature effects on the phase behavior of phospholipid bilayers. For example, the increase of the temperature results in the melting of the DPPC bilayer (53), as shown by the comparison of the lipid diffusion at 300 and 330 K (Fig. S4).

Mechanical properties of the DPPC and POPC monolayers

From the slopes of the pressure-area isotherms, we can obtain the area compressibility modulus Cs^{-1}, which is the reciprocal of the compressibility Cs and equivalent to elasticity. The compressibility can be expressed as

$$Cs = -\frac{1}{A}\left(\frac{\partial A}{\partial \pi}\right)_T, \tag{6}$$

where A and π are the APL and surface pressure, respectively. A typical area compressibility modulus of DPPC monolayers measured via experiments and simulations is in the range of 10–50 mN/m in the LE phase and 100–250 mN/m in the LC phase (12,15,53,54). We summarize our simulated and experimental data as well as the data in the existing literature in Table 4. The area compressibility moduli of the LC and LE phases of the monolayer are approximated by linear regression from the pressure-area isotherm. The calculated compressibility modulus of the MDPD DPPC monolayer in the LC phase is close to the Martini simulations (12) and is much larger than the

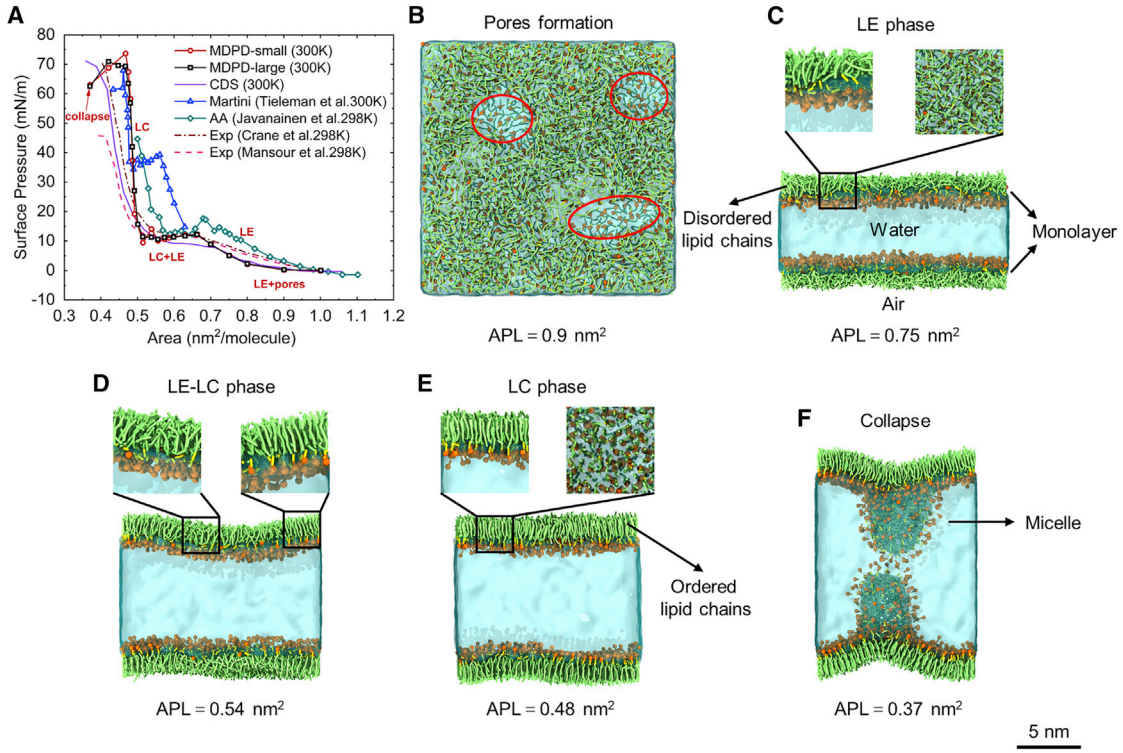

Figure360▷ FIGURE 2 For a Figure360 author presentation of this figure, see https://doi.org/10.1016/j.bpj.2021.09.031. (*A*) Surface pressure-area isotherms of pure DPPC monolayers from MDPD simulations and CDS experiments compared to the literature data, including AAMD (54), Martini simulations (12), and experiments (15,53). Note that the isotherm in Martini simulations is corrected by shifting along the *y* axis. (*B*) Top view of the pore formation in the DPPC monolayer in the small system. (*C*) Side view of DPPC monolayers in nonporous LE phase with the enlarged local structure for disordered tail lipid chains at the side and top views. (*D*) Side view of DPPC monolayers in LE-LC coexistence phase with the enlarged local structure for disordered tail lipid chains (LE phase) and ordered tail lipid chains (LC phase) at the side view. (*E*) Side view of DPPC monolayer in LC phase with the enlarged local structure for ordered tail lipid chains at the side and top views. (*F*) Side view of the DPPC monolayer collapsed to form micelles in the water phase. The corresponding APLs are given below the snapshots. To see this figure in color, go online.

experimental results (15,53) and AAMD simulations (54), whereas that in the LE phase is more closed to experimental results and the AAMD simulations than Martini simulations. Because of the high rigidity of the LC phase, the lipid diffusion in the LC phase is orders of magnitude lower than that in the LE phase, which is consistent with the previous experimental data (66) (Fig. S5). The POPC monolayer is mainly at the LE phase in the APL range of 0.55–1.0 nm^2, and the slope of the isotherm obviously changes at such a range. Thus, the calculated compressibility modulus of the POPC ranges from 30 to 85 mN/m in relation to the APL and the calculated values are similar to the CDS experiments as well as previous experiments (62–64) and AAMD simulations (54). At the same APL, the modulus of the POPC monolayer is much smaller than that of the DPPC monolayer, which is in accordance with the experimental results.

Molecular structures of the DPPC and POPC monolayers

During expression and expansion, the lipid monolayer at the air-water interface exhibits different molecular structures. In this section, we examine the molecular structures of the DPPC and POPC monolayers at different stages. First, we show the molecular structure transformation of the DPPC and POPC monolayers at the rupture and collapse stages under the extremely high and low surface tension in Fig. 5.

For the DPPC monolayer, the pore formation of the monolayer starts at APL = 0.9 nm^2 with stable pores, and these pores grow with an increase in the APL to 1.0 nm^2. Formation of pores was also confirmed by the AAMD simulation at APL = 1.1 nm^2 (54) and the existing experiment at APL = 1.1 nm^2 (67). Considering the possible deviation of the operating conditions in experiments and the intrinsic uncertainty involved in molecular simulations, we feel that the difference of the pore formation between our study and the other results is acceptable. Compared to the DPPC monolayer, the POPC monolayer is more stable at high surface tension and starts to form pores at APL = 1.0 nm^2. This is because the work of formation of a round pore of radius r equals $2\pi r\Gamma - \pi r^2\sigma$ (Γ is the line tension at the edge of the pore and σ is the surface tension) (68), and the POPC molecule has a larger line tension because of the unsaturated bead. At the collapse stage, the

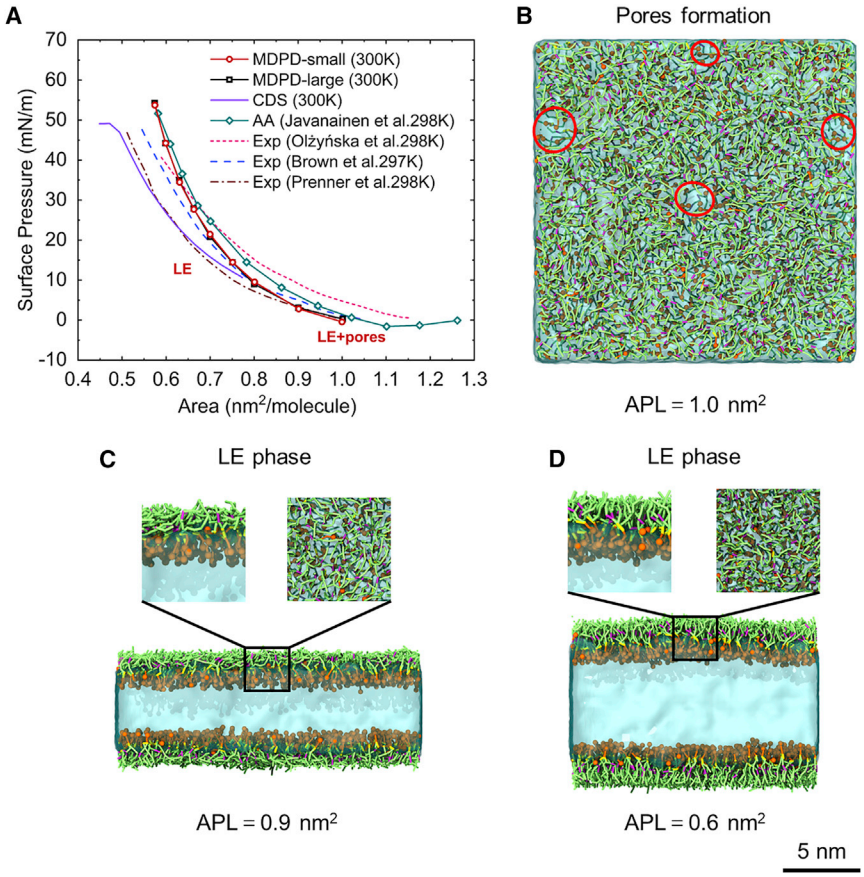

FIGURE 3 (*A*) Comparison of surface pressure-area isotherms of pure POPC monolayers from these MDPD simulations, CDS experiments, AAMD simulations (54), and others' experiments (60–62). (*B*) Top view of the hole formation in the POPC monolayer. (*C* and *D*) Side views of POPC monolayers with disordered lipid tail chains at different APLs of the LE phase. To see this figure in color, go online.

DPPC monolayer collapses from the small undulations, and DPPC molecules are extruded to form the bilayer structure in the water phase, which is similar to the previous CGMD simulations (69). In addition, the structure transformation between the DPPC molecules in the water phase and at the air-water interface is governed by the surface pressure of the DPPC monolayer as revealed by the previous experiment (53). This model also demonstrated that the DPPC molecules in the water phase could adsorb to the DPPC monolayer at the air-water interface if the surface pressure is below the equilibrium surface pressure of the monolayer (~45 mN/m), whereas such adsorption was inhibited under the surface pressure larger than the equilibrium surface pressure, as shown in Fig. S6. However, the desorption of the lipids was not observed in our simulations when the surface tension was above 45 mN/m, which was possibly caused by the high compressibility of the DPPC monolayer.

Except for the rupture and collapse stages, although the lipid monolayer is always flat under expression and expansion, it exhibits different molecular structures at the different surface tensions. The order parameter of the lipid tails is an important property to quantitatively describe the orientation of the lipids and the phase separation. It is defined as (20)

$$S_z = \frac{3}{2}\langle \cos^2\theta_n \rangle - \frac{1}{2}, \tag{7}$$

where θ_n is the angle between the calculated molecular axis connecting the n − 1 and n + 1 sites of the hydrocarbon chain and the normal z axis of the monolayer. At a low surface tension (APL = 0.45, 0.47 nm^2), the DPPC monolayer is in the LC phase and the corresponding order parameter is much larger than in the LE phase (APL ≥ 0.63 nm^2) as shown in Fig. 6 *A*. These calculated average values of the order parameter are quantitatively in line with the Martini CGMD simulations (12). Besides, the DPPC tails in the LC phase exhibit an averaged tilt of ~26.34° (Fig. S7) that agrees well with the previous experimental measurement of 25° (70). It should be noted that the collective tilt of the DPPC chains in the LC phase is still hardly observed. This is similar to the previous Martini simulations (12,71) but different from other DPD simulations (72). The POPC monolayer has a bond angle of 120° in the unsaturated tail chain, thus leading to an obvious decrease in the order parameter in the sn-1 tail (Fig. 6 *B*). Generally, the order parameters of the POPC monolayer are much smaller than those of the DPPC monolayer at the same APL. The bead density

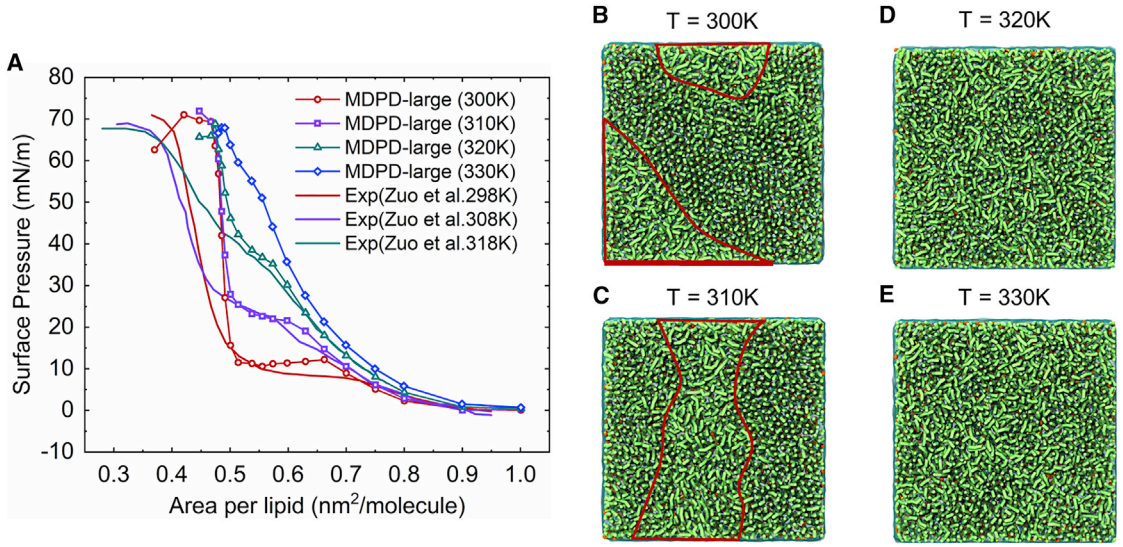

FIGURE 4 (*A*) Comparison of surface pressure-area isotherms of pure DPPC monolayers at different temperatures (300, 310, 320, and 330 K) from these MDPD simulations and the existing experiment (63). Top view of DPPC monolayers at APL = 0.57 nm^2 at 300 K (*B*), 310 K (*C*), 320 K (*D*), and 330 K (*E*) is shown. The LE phase coexistence is surrounded by red lines for clarity in (*B*) and (*C*). To see this figure in color, go online.

distributions of the monolayer at the z axis (Fig. S8) shows that the DPPC monolayer is little thinner than the POPC monolayer at the same APL. This indicates that the POPC molecules are more likely to be arranged in parallel at the air-water interface, which is in accordance with the order parameters. We also notice that there is an obvious

TABLE 4 Experimental and simulated area compressibility moduli

	Temperature (K)	Phase	Cs^{-1} (mN/m)	Area (Å^2)
DPPC monolayers	Varies			Varies
MDPD large	300	LC	~894	~48.5
MDPD small	300	LC	~835	~48.5
CDS	300	LC	~378	~43.6
Tieleman et al. (12) (Martini)	300	LC	~786	~47.6
Javanainen et al. (54) (AAMD)	298	LC	~315	~50.2
Crane et al. (15) (Exp)	298	LC	~272	~45.0
Mansour et al. (53) (Exp)	298	LC	~215	~46.2
MDPD large	300	LE	~50	~70
MDPD small	300	LE	~51	~70
CDS	300	LE	~36	~75
Tieleman et al. (12) (Martini)	300	LE	~243	~58.9
Javanainen et al. (54) (AAMD)	298	LE	~58	~78.2
Crane et al. (15) (Exp)	298	LE	~32	~79.7
Mansour et al. (53) (Exp)	298	LE	~34	~74.5
POPC monolayers	Varies			Varies
MDPD large	300	LE	~164	~62.9
	300	LE	~53	~80
MDPD small	300	LE	~164	~62.9
	300	LE	~53	~80
CDS	300	LE	~110	~52
	300	LE	~58	~70
Javanainen et al. (54) (AAMD)	298	LE	~153	~67.2
	298	LE	~58	~86.2
Olżyńska et al. (60) (Exp)	298	LE	~86	~60
	298	LE	~38	~90
Brown et al. (61) (Exp)	297	LE	~114	~58
	297	LE	~45	~90
Prenner et al. (62) (Exp)	298	LE	~119	~55
	298	LE	~47	~80

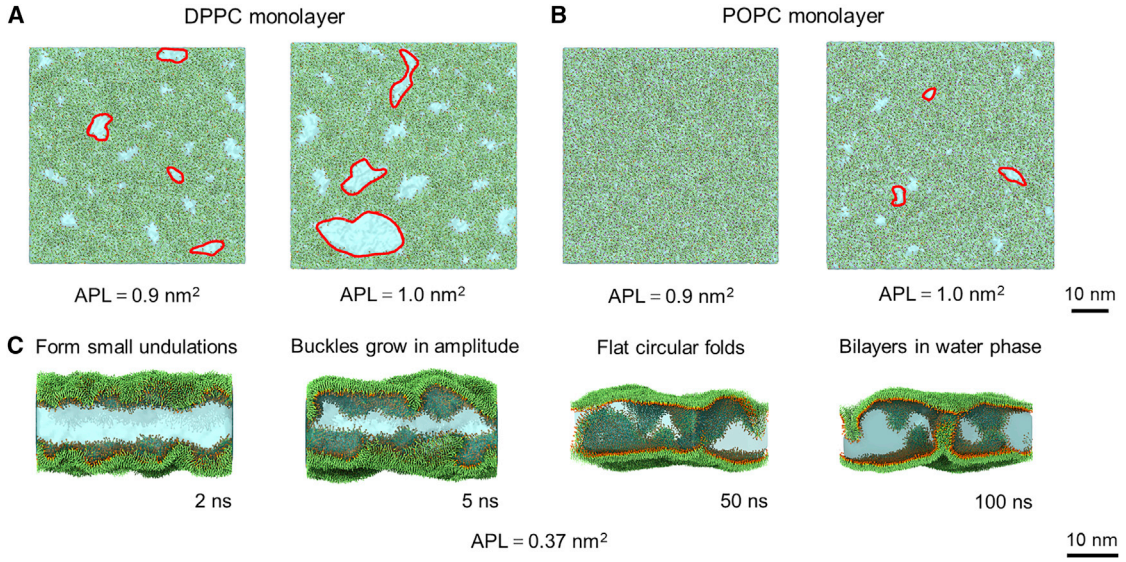

FIGURE 5 Snapshots for the simulations of DPPC monolayers in the large system at the collapse and rupture stages. (*A* and *B*) Pore formation of DPPC and POPC monolayers at APL = 0.9 and 1.0 nm^2, respectively, in the top view. (*C*) Structure transformation of the DPPC monolayer at the collapse stage: forming small undulations (*top left*), buckling grows (*top right*), and the monolayers collapse, forming extruded bilayers in the water phase (*bottom right* and *bottom left*). To see this figure in color, go online.

hydration layer near the headgroups by examining the water distribution along the headgroups of the monolayer (Fig. S9).

Pressure-area isotherms of mixed DPPC/POPC monolayers

The natural lung surfactant monolayer has complex and unique biophysical properties because of its complex lipid composition. Therefore, modeling toward the real multicomponent lipid monolayer is crucial for understanding the biophysics of the lung surfactant monolayer. Next, we study the experimental and simulated isotherms of three mixed DPPC/POPC monolayers of different ratios, as shown in Fig. 7. The isotherms of the simulated and experimental mixed DPPC/POPC monolayers are between the isotherms of the pure DPPC and POPC monolayers. With the increase in the ratio of POPC, the LE-LC coexistence phase plateau of isotherms of the mixed monolayer gradually disappeared, and the slope at the low APLs decreased as well. When the mixed ratio is larger than 50%, the shape of the simulated isotherms of the mixed monolayers is

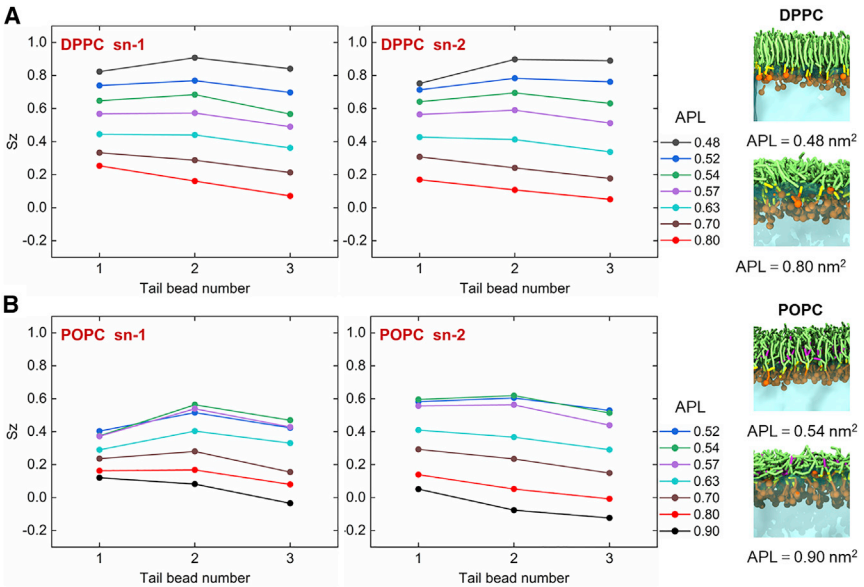

FIGURE 6 Order parameters of tail beads in the DPPC (*A*) and POPC (*B*) monolayers at various APLs and the typical snapshots for the molecular structure at different APLs. The bead numbers stand for the bead series in the tails, in which 1, 2, and 3 are the second, third, and fourth bead in each tail, respectively. The first bead and the last bead in each tail were not included in the calculation of order parameter. To see this figure in color, go online.

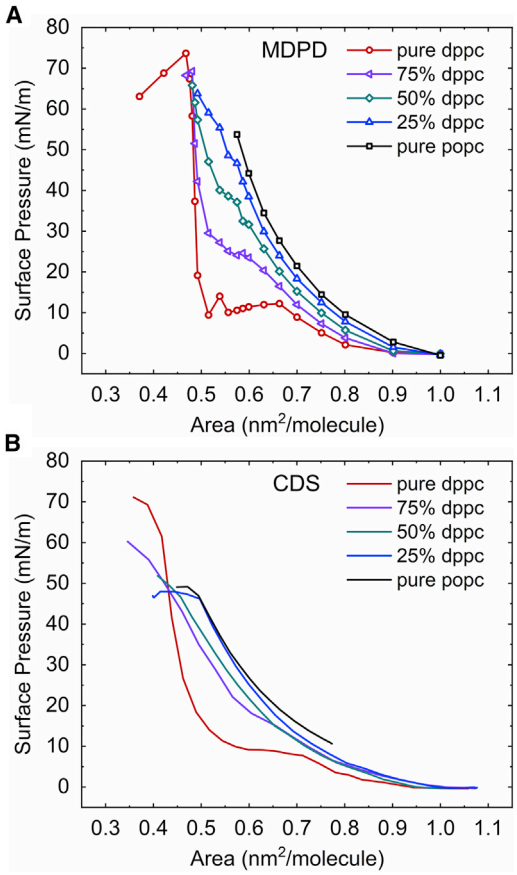

FIGURE 7 Surface pressure-area isotherms of three mixed DPPC/POPC monolayers and pure (DPPC or POPC) monolayers obtained by the MDPD simulations (*A*) and the CDS experiments (*B*). The mixing ratio of DPPC molecules in the mixed monolayers was set to 25, 50, and 75%. To see this figure in color, go online.

essentially similar to the that of the pure POPC monolayer without an obvious plateau, which manifests the same trend as our CDS experiment and the existing experiment (73). Therefore, these MDPD models are promising in capturing the important feature of the mixed monolayers, for example, a shift from an isotherm with a plateau to that without a plateau depending on the ratio of DPPC/POPC molecules. However, it should be noted that at an APL <0.5 nm^2, the calculated isotherms of mixed monolayer have a larger slope with a steep increase in the pressure, whereas the pressure in the experimental isotherms slowly increases, leading to a slight deviation in the compressibility between the simulations and experiments. Generally, our model is capable of capturing the features of the mixed lipid monolayer, and the parameterization scheme could be applied to more types of phospholipids, which can be used to mimic the mesoscopic behavior of natural lipid monolayers.

It should be noted that although our MDPD model can quantitatively simulate the phospholipid monolayers at the mesoscale, there are still some limitations. First, for simulating a large system of DPPC monolayers with a horizontal size of 60 $\times$ 60 nm and a total bead number of 366,000, it takes $\sim$1.05 h to run 1,000,000 steps on 720 CPU cores in 30 nodes (320 ns). Although this MDPD took only quarter of the computing time for the Martini CGMD with a similar simulation system (Table S1), our simulation scale is limited to hundreds of nanometers and microseconds. Second, our MDPD model does not include any electrostatic interactions. Third, the bond and angle parameters refer to previous DPD lipid models and are worth optimizing for more accurate monolayer simulations.

CONCLUSIONS

Although phospholipid monolayers at the air-water interface have been widely studied using experimental and computational methods, it is still difficult to quantitatively model the physical properties of the phospholipid monolayers at the mesoscopic scale. Here, we present an MDPD model for two commonly used phospholipids, DPPC and POPC. Using a parameterization scheme based on mapping the calculated physical properties to the experimental values, we reproduced the pressure-area isotherms of the phospholipid monolayers in MDPD simulations with a good fitting to our CDS experiments. In addition, the mechanical properties and molecular structures of phospholipid monolayers were quantitatively and qualitatively in line with the experiments and AAMD simulations. This model can also capture the sensitive changes in the pressure isotherms of the mixed DPPC/POPC monolayers by altering the mixing ratios of the components. These results demonstrated that our model can be applied for mesoscale phospholipid simulations at the air-water interface with molecular resolution but less computing cost.

SUPPORTING MATERIAL

Supporting material can be found online at https://doi.org/10.1016/j.bpj.2021.09.031.

AUTHOR CONTRIBUTIONS

G.H. and X.B. designed the research. Y.Z. performed the simulations and experiments. Y.Z. and X.B. analyzed and interpreted the data. X.B., Y.Z., and G.H. wrote the manuscript.

ACKNOWLEDGMENTS

We thank the reviewers for providing many constructive suggestions that helped us improve this manuscript.

This work was supported financially by the National Natural Science Foundation of China (11832017), the Chinese Academy of Sciences Key Research Program of Frontier Sciences (QYZDB-SSW-JSC036), the Chinese Academy of Sciences Strategic Priority Research Program (XDB22040403), and the China National Postdoctoral Program for

Innovative Talents (BX20200298). The numerical simulations were performed on TianHe-1(A) at the National Supercomputing Center in Tianjin.

SUPPORTING CITATIONS

Reference (74) appears in the Supporting material.

REFERENCES

1. Gruen, D. W., and J. Wolfe. 1982. Lateral tensions and pressures in membranes and lipid monolayers. *Biochim. Biophys. Acta.* 688:572–580.
2. Jähnig, F. 1984. Lipid exchange between membranes. *Biophys. J.* 46:687–694.
3. Nagle, J. F. 1986. Theory of lipid monolayer and bilayer chain-melting phase transitions. *Faraday Discuss. Chem. Soc.* 81:151–162.
4. Feng, S. S. 1999. Interpretation of mechanochemical properties of lipid bilayer vesicles from the equation of state or pressure-area measurement of the monolayer at the air-water or oil-water interface. *Langmuir.* 15:998–1010.
5. Goerke, J. 1974. Lung surfactant. *Biochim. Biophys. Acta.* 344:241–261.
6. Marsh, D. 1996. Lateral pressure in membranes. *Biochim. Biophys. Acta.* 1286:183–223.
7. Schindler, H. 1979. Exchange and interactions between lipid layers at the surface of a liposome solution. *Biochim. Biophys. Acta.* 555:316–336.
8. Walters, R. W., R. R. Jenq, and S. B. Hall. 2000. Distinct steps in the adsorption of pulmonary surfactant to an air-liquid interface. *Biophys. J.* 78:257–266.
9. Bai, X., L. Xu, …, G. Hu. 2019. Adsorption of phospholipids at the air-water surface. *Biophys. J.* 117:1224–1233.
10. Alonso, C., T. Alig, …, J. A. Zasadzinski. 2004. More than a monolayer: relating lung surfactant structure and mechanics to composition. *Biophys. J.* 87:4188–4202.
11. Parra, E., and J. Pérez-Gil. 2015. Composition, structure and mechanical properties define performance of pulmonary surfactant membranes and films. *Chem. Phys. Lipids.* 185:153–175.
12. Baoukina, S., L. Monticelli, …, D. P. Tieleman. 2007. Pressure-area isotherm of a lipid monolayer from molecular dynamics simulations. *Langmuir.* 23:12617–12623.
13. Zhang, H., Q. Fan, …, Y. Y. Zuo. 2011. Comparative study of clinical pulmonary surfactants using atomic force microscopy. *Biochim. Biophys. Acta.* 1808:1832–1842.
14. Langmuir, I. 1916. The constitution and fundamental properties of solids and liquids. Part I. Solids. *J. Am. Chem. Soc.* 38:2221–2295.
15. Crane, J. M., G. Putz, and S. B. Hall. 1999. Persistence of phase coexistence in disaturated phosphatidylcholine monolayers at high surface pressures. *Biophys. J.* 77:3134–3143.
16. Ahuja, R. C., and D. Mobius. 1992. Photophysical properties of a pyrene-labeled phospholipid in matrix monolayers at the gas/water interface. *Langmuir.* 8:1136–1144.
17. Baldyga, D. D., and R. A. Dluhy. 1998. On the use of deuterated phospholipids for infrared spectroscopic studies of monomolecular films: a thermodynamic analysis of single and binary component phospholipid monolayers. *Chem. Phys. Lipids.* 96:81–97.
18. Duncan, S. L., I. S. Dalal, and R. G. Larson. 2011. Molecular dynamics simulation of phase transitions in model lung surfactant monolayers. *Biochim. Biophys. Acta.* 1808:2450–2465.
19. Zhang, S., and X. Lin. 2019. Lipid acyl chain *cis* double bond position modulates membrane domain registration/anti-registration. *J. Am. Chem. Soc.* 141:15884–15890.
20. Baoukina, S., E. Mendez-Villuendas, and D. P. Tieleman. 2012. Molecular view of phase coexistence in lipid monolayers. *J. Am. Chem. Soc.* 134:17543–17553.
21. Kaznessis, Y. N., S. Kim, and R. G. Larson. 2002. Simulations of zwitterionic and anionic phospholipid monolayers. *Biophys. J.* 82:1731–1742.
22. Yang, K., and Y. Q. Ma. 2010. Computer simulation of the translocation of nanoparticles with different shapes across a lipid bilayer. *Nat. Nanotechnol.* 5:579–583.
23. Vanommeslaeghe, K., E. Hatcher, …, A. D. Mackerell, Jr. 2010. CHARMM general force field: a force field for drug-like molecules compatible with the CHARMM all-atom additive biological force fields. *J. Comput. Chem.* 31:671–690.
24. Marrink, S. J., H. J. Risselada, …, A. H. de Vries. 2007. The MARTINI force field: coarse grained model for biomolecular simulations. *J. Phys. Chem. B.* 111:7812–7824.
25. Marrink, S. J., and D. P. Tieleman. 2013. Perspective on the Martini model. *Chem. Soc. Rev.* 42:6801–6822.
26. Hoogerbrugge, P. J., and J. M. V. A. Koelman. 1992. Simulating microscopic hydrodynamic phenomena with dissipative particle dynamics. *Europhys. Lett.* 19:155–160.
27. Baoukina, S., and D. P. Tieleman. 2013. Simulations of lipid monolayers. *In* Biomolecular Simulations: Methods and Protocols. L. Monticelli and E. Salonen, eds. Springer, pp. 431–444.
28. Shinoda, W., R. DeVane, and M. L. Klein. 2010. Zwitterionic lipid assemblies: molecular dynamics studies of monolayers, bilayers, and vesicles using a new coarse grain force field. *J. Phys. Chem. B.* 114:6836–6849.
29. Shinoda, W., R. Devane, and M. L. Klein. 2007. Multi-property fitting and parameterization of a coarse grained model for aqueous surfactants. *Mol. Simul.* 33:27–36.
30. Chiu, S. W., H. L. Scott, and E. Jakobsson. 2010. A coarse-grained model based on morse potential for water and n-alkanes. *J. Chem. Theory Comput.* 6:851–863.
31. Groot, R. D., and K. L. Rabone. 2001. Mesoscopic simulation of cell membrane damage, morphology change and rupture by nonionic surfactants. *Biophys. J.* 81:725–736.
32. Shi, X. H., and F. L. Tian. 2019. Multiscale modeling and simulation of nano-carriers delivery through biological barriers-a review. *Adv. Theory Simul.* 2:1800105.
33. Español, P., and P. B. Warren. 2017. Perspective: dissipative particle dynamics. *J. Chem. Phys.* 146:150901.
34. Trofimov, S. Y., E. L. F. Nies, and M. A. J. Michels. 2002. Thermodynamic consistency in dissipative particle dynamics simulations of strongly nonideal liquids and liquid mixtures. *J. Chem. Phys.* 117:9383–9394.
35. Warren, P. B. 2003. Vapor-liquid coexistence in many-body dissipative particle dynamics. *Phys. Rev. E Stat. Nonlin. Soft Matter Phys.* 68:066702.
36. Chu, K. C., S. W. Hu, …, Y. J. Sheng. 2019. Strong competition between adsorption and aggregation of surfactant in nanoscale systems. *J. Colloid Interface Sci.* 553:674–681.
37. Zhou, P., J. Hou, …, W. Chen. 2019. Effect of aggregation and adsorption behavior on the flow resistance of surfactant fluid on smooth and rough surfaces: a many-body dissipative particle dynamics study. *Langmuir.* 35:8110–8120.
38. Warren, P. B. 2013. No-go theorem in many-body dissipative particle dynamics. *Phys. Rev. E Stat. Nonlin. Soft Matter Phys.* 87:045303.
39. Espanol, P., and P. Warren. 1995. Statistical-mechanics of dissipative particle dynamics. *Europhys. Lett.* 30:191–196.
40. Marrink, S. J., A. H. de Vries, and A. E. Mark. 2004. Coarse grained model for semiquantitative lipid simulations. *J. Phys. Chem. B.* 108:750–760.
41. Li, Y., H. Yuan, …, H. Gao. 2013. Graphene microsheets enter cells through spontaneous membrane penetration at edge asperities and corner sites. *Proc. Natl. Acad. Sci. USA.* 110:12295–12300.

42. Martínez, L., R. Andrade, …, J. M. Martínez. 2009. PACKMOL: a package for building initial configurations for molecular dynamics simulations. *J. Comput. Chem.* 30:2157–2164.

43. Irving, J., and J. G. Kirkwood. 1950. The statistical mechanical theory of transport processes. IV. The equations of hydrodynamics. *J. Chem. Phys.* 18:817–829.

44. Li, Z., G. H. Hu, …, Z. W. Zhou. 2013. Three dimensional flow structures in a moving droplet on substrate: a dissipative particle dynamics study. *Phys. Fluids.* 25:072103.

45. Plimpton, S. 1995. Fast parallel algorithms for short-range molecular-dynamics. *J. Comput. Phys.* 117:1–19.

46. Humphrey, W., A. Dalke, and K. Schulten. 1996. VMD: visual molecular dynamics. *J. Mol. Graph.* 14:33–38, 27–28.

47. Valle, R. P., T. Wu, and Y. Y. Zuo. 2015. Biophysical influence of airborne carbon nanomaterials on natural pulmonary surfactant. *ACS Nano.* 9:5413–5421.

48. Yu, K., J. Yang, and Y. Y. Zuo. 2016. Automated droplet manipulation using closed-loop axisymmetric drop shape analysis. *Langmuir.* 32:4820–4826.

49. Yang, J., K. Yu, and Y. Y. Zuo. 2017. Accuracy of axisymmetric drop shape analysis in determining surface and interfacial tensions. *Langmuir.* 33:8914–8923.

50. Ghoufi, A., and P. Malfreyt. 2011. Mesoscale modeling of the water liquid-vapor interface: a surface tension calculation. *Phys. Rev. E Stat. Nonlin. Soft Matter Phys.* 83:051601.

51. Yeh, I. C., and G. Hummer. 2004. System-size dependence of diffusion coefficients and viscosities from molecular dynamics simulations with periodic boundary conditions. *J. Phys. Chem. B.* 108:15873–15879.

52. Queimada, A. J., I. M. Marrucho, …, E. H. Stenby. 2005. Viscosity and liquid density of asymmetric n-alkane mixtures: measurement and modeling. *Int. J. Thermophys.* 26:47–61.

53. Mansour, H. M., and G. Zografi. 2007. Relationships between equilibrium spreading pressure and phase equilibria of phospholipid bilayers and monolayers at the air-water interface. *Langmuir.* 23:3809–3819.

54. Javanainen, M., A. Lamberg, …, O. H. Samuli Ollila. 2018. Atomistic model for nearly quantitative simulations of Langmuir monolayers. *Langmuir.* 34:2565–2572, Published online October 10, 2017.

55. Castro-Román, F., R. W. Benz, …, D. J. Tobias. 2006. Investigation of finite system-size effects in molecular dynamics simulations of lipid bilayers. *J. Phys. Chem. B.* 110:24157–24164.

56. Mauk, A. W., E. L. Chaikof, and P. J. Ludovice. 1998. Structural characterization of self-assembled lipid monolayers by N π T simulation. *Langmuir.* 14:5255–5266.

57. Duncan, S. L., and R. G. Larson. 2008. Comparing experimental and simulated pressure-area isotherms for DPPC. *Biophys. J.* 94:2965–2986.

58. de Vries, A. H., I. Chandrasekhar, …, P. H. Hünenberger. 2005. Molecular dynamics simulations of phospholipid bilayers: influence of artificial periodicity, system size, and simulation time. *J. Phys. Chem. B.* 109:11643–11652.

59. Lindahl, E., and O. Edholm. 2000. Mesoscopic undulations and thickness fluctuations in lipid bilayers from molecular dynamics simulations. *Biophys. J.* 79:426–433.

60. Olzynska, A., M. Zubek, …, L. Cwiklik. 2016. Mixed DPPC/POPC monolayers: all-atom molecular dynamics simulations and Langmuir monolayer experiments. *Biochim. Biophys. Acta.* 1858:3120–3130.

61. Brown, R. E., and H. L. Brockman. 2007. Using monomolecular films to characterize lipid lateral interactions. *Methods Mol. Biol.* 398:41–58.

62. Prenner, E., G. Honsek, …, K. Lohner. 2007. Imaging of the domain organization in sphingomyelin and phosphatidylcholine monolayers. *Chem. Phys. Lipids.* 145:106–118.

63. Zuo, Y. Y., R. Chen, …, A. W. Neumann. 2016. Phase transitions in dipalmitoylphosphatidylcholine monolayers. *Langmuir.* 32:8501–8506.

64. Phillips, M. C., and D. Chapman. 1968. Monolayer characteristics of saturated 1,2,-diacyl phosphatidylcholines (lecithins) and phosphatidylethanolamines at the air-water interface. *Biochim. Biophys. Acta.* 163:301–313.

65. Kodama, M., O. Shibata, …, G. Sugihara. 2004. A monolayer study on three binary mixed systems of dipalmitoyl phosphatidyl choline with cholesterol, cholestanol and stigmasterol. *Colloids Surf. B Biointerfaces.* 33:211–226.

66. Peters, R., and K. Beck. 1983. Translational diffusion in phospholipid monolayers measured by fluorescence microphotolysis. *Proc. Natl. Acad. Sci. USA.* 80:7183–7187.

67. Roke, S., J. Schins, …, M. Bonn. 2003. Vibrational spectroscopic investigation of the phase diagram of a biomimetic lipid monolayer. *Phys. Rev. Lett.* 90:128101.

68. Burgess, S., A. Vishnyakov, …, A. V. Neimark. 2018. Nanoparticle-engendered rupture of lipid membranes. *J. Phys. Chem. Lett.* 9:4872–4877.

69. Baoukina, S., L. Monticelli, …, D. P. Tieleman. 2008. The molecular mechanism of lipid monolayer collapse. *Proc. Natl. Acad. Sci. USA.* 105:10803–10808.

70. Ma, G., and H. C. Allen. 2006. DPPC Langmuir monolayer at the air-water interface: probing the tail and head groups by vibrational sum frequency generation spectroscopy. *Langmuir.* 22:5341–5349.

71. Sharma, P., R. Desikan, and K. G. Ayappa. 2021. Evaluating coarse-grained MARTINI force-fields for capturing the ripple phase of lipid membranes. *J. Phys. Chem. B.* 125:6587–6599.

72. Rodgers, J. M., J. Sørensen, …, B. Smit. 2012. Understanding the phase behavior of coarse-grained model lipid bilayers through computational calorimetry. *J. Phys. Chem. B.* 116:1551–1569.

73. Torrent-Burgues, J. 2018. Thermodynamic behaviour of mixed films of an unsaturated and a saturated polar lipid. (Oleic acid-stearic acid and POPC-DPPC). *Colloids Ints.* 2:17.

74. Van Der Spoel, D., E. Lindahl, …, H. J. Berendsen. 2005. GROMACS: fast, flexible, and free. *J. Comput. Chem.* 26:1701–1718.